

A Poroelastic Immersed Boundary Method with Applications to Cell Biology

Wanda Strychalski^{a,*}, Calina A. Copos^b, Owen L. Lewis^b, Robert D. Guy^b

^a*Department of Mathematics, Applied Mathematics, and Statistics, Case Western Reserve University, Cleveland, OH 44106*

^b*Department of Mathematics, University of California, Davis, CA 95616*

Abstract

The immersed boundary method is a widely used mixed Eulerian/Lagrangian framework for simulating the motion of elastic structures immersed in viscous fluids. In the traditional immersed boundary method, the fluid and structure move with the same velocity field. In this work, a model based on the immersed boundary method is presented for simulating poroelastic media in which the fluid permeates a porous, elastic structure of small volume fraction that moves with its own velocity field. Two distinct methods for calculating elastic stresses are presented and compared. The method is validated on a radially symmetric test problem by comparing with a finite difference solution of the classical equations of poroelasticity. Finally, two applications of the modeling framework to cell biology are provided: cellular blebbing and cell crawling. It is shown that in both examples, poroelastic effects are necessary to explain the relevant mechanics.

Keywords: fluid-structure interaction, stokes flow, hyperelasticity, cell crawling, blebbing

1. Introduction

The immersed boundary (IB) method is a computational method for simulating fluid-structure interaction problems. It has been applied to many biological and physical systems such as blood flow in the heart [1], insect flight [2], and flagellar swimming [3]. In the traditional IB method, the elastic structure moves with the local fluid velocity. The method has been adapted for porous membranes in which the fluid moves through the elastic structure [4, 5], and this variant has been applied to problems such as parachute mechanics [4] and suction feeding in jellyfish [6]. However, the porous IB method has been limited

*Corresponding Author

Email addresses: wis6@case.edu (Wanda Strychalski), ccopos@math.ucdavis.edu (Calina A. Copos), ollewis@math.ucdavis.edu (Owen L. Lewis), guy@math.ucdavis.edu (Robert D. Guy)

to infinitely thin elastic membranes. IB methods have been extended to thick elastic structures, but only for the case when the structure moves with the local fluid velocity [7–9]. Many biological materials, such as the cell cytoplasm [10], brain tissue [11], and blood clots [12], involve immersed structures that are both elastic and porous. In this paper, we are motivated by poroelasticity of the cytoplasm and how its material properties affect cell processes driven by fluid dynamics.

The cytoplasm is the intracellular mixture of organelles, the cytosol, and the cytoskeleton [13]. The cytosol is the liquid portion of the cytoplasm consisting of water, ions, and dissolved molecules. The cytoskeleton is a system of protein filaments in the cytoplasm that give the cell its shape and ability to move. Actin filaments are a major cytoskeletal component that play an important role in cell motility. The cytoplasm has been modeled on the continuum level as an elastic material, viscoelastic material, porous gel, and viscous fluid [14–16]. The appropriate rheological description of the cytoplasm depends on the timescale and relevant cellular under consideration. For example, actin filaments depolymerize and repolymerize on a timescale of minutes. Therefore, an actin network behaves like an elastic material on the timescale of seconds, but a fluid on timescales longer than minutes.

Recent work suggests that cytoplasmic streaming plays an important role in cell motility [17]. The rheological properties of the cytoplasm affect pressure propagation and fluid flow in migrating cells that exhibit cytoplasmic streaming. Some animal cells use blebs, spherical membrane protrusions driven by cytoplasmic flow, for migration [18]. In [19], the authors found cytoplasmic elasticity necessary to limit bleb size. Other recent blebbing experiments support the view of the cytoplasm as a poroelastic material [10]. The relative motion of the cytosol flowing through the cytoskeleton demonstrates that the cytoplasm acts as a two-phase material in blebbing cells. Similarly, in large amoeboid cells, relative motion between cytoplasmic phases has been observed in *Amoeba proteus* [20] and *Physarum polycephalum* [21]. In *Physarum polycephalum* cells, cytoplasmic streaming driven by cytoskeletal contraction corresponds with an increase in cell migration speed [21], which suggests that cytoplasmic streaming drives locomotion. Generally, the role of fluid mechanics in cells that use cytoplasmic streaming for migration is not fully understood.

Motivated by problems involving cytoplasmic streaming and cell locomotion, we propose a novel method for simulating poroelastic structures in a mixed Eulerian/Lagrangian framework. In our formulation, there is a separate force balance equation for fluid and for the elastic structure, and the two materials are coupled through drag forces. We show that our formulation agrees with the traditional Eulerian formulation of poroelasticity. Elastic forces within the structure are computed using two different methods. The first method extends lattice-spring models, in which elastic structures are discretized by a network of springs, to unstructured grids. We also used the energy-based method for describing hyperelastic materials from [9]. The method is applied to models of cellular blebbing and cell crawling, where we demonstrate the properties of both the fluid and structure are necessary to capture the relevant biological

behavior.

2. Mathematical Formulation

To describe the mechanics of poroelastic materials, we begin with the two-phase flow model [22], which is often used to describe multicomponent mixtures that consist of an elastic network immersed in a viscous fluid. Each phase moves with its own velocity field and at any given point, the composition of the mixture is described by the volume fractions of the different phases. The velocity of the fluid is denoted by \mathbf{u}_f and the network velocity by \mathbf{u}_n . The volume fraction of the network phase is ϕ and it is assumed to be constant. Since the volume fractions sum to one, the volume fraction of the fluid is $1 - \phi$. For constant density, mass conservation leads to volume averaged incompressibility. For applications in cell biology, the Reynolds number is very small and inertial forces may be neglected. Then, the force density balance for each phase and the volume averaged incompressibility constraint are given by

$$\nabla \cdot \sigma_f - (1 - \phi) \nabla p + \xi (\mathbf{u}_n - \mathbf{u}_f) = 0 \quad (\text{fluid}) \quad (1)$$

$$\nabla \cdot \sigma_e - \phi \nabla p + \xi (\mathbf{u}_f - \mathbf{u}_n) = 0 \quad (\text{network}) \quad (2)$$

$$\nabla \cdot (\phi \mathbf{u}_n + (1 - \phi) \mathbf{u}_f) = 0, \quad (\text{mixture incompressibility}) \quad (3)$$

where the σ_i 's indicate fluid and elastic stress tensors, p is the pressure, and ξ is the drag coefficient between the network and the fluid. The elastic stress tensor σ_e is given by the appropriate constitutive law (provided in the next section). For a Newtonian fluid, the fluid stress is given by

$$\sigma_f = \mu (\nabla \mathbf{u}_f + \nabla \mathbf{u}_f^T) + \lambda (\nabla \cdot \mathbf{u}_f) \mathcal{I}, \quad (4)$$

where μ is the shear fluid viscosity and λ is the second coefficient of viscosity.

We note here that by assuming that σ_f is negligible, one can derive the standard model of poroelastic media given in [23]. By adding (1) and (2), the drag term can be eliminated from the network force density balance. Similarly, rearrangement of (1) results in a Darcy law governing the fluid. This yields the system

$$\nabla \cdot \sigma_e - \nabla p = 0 \quad (5)$$

$$\mu (\mathbf{u}_f - \mathbf{u}_n) = -\kappa \nabla p. \quad (6)$$

Here the quantity $\kappa = \mu(1 - \phi)/\xi$ is interpreted as the Darcy permeability of the network. Indeed, for materials of known permeability, we calculate the drag parameter using $\xi = \mu(1 - \phi)/\kappa$. This technique is used for numerical simulations performed in Section 4. Because we wish to investigate problems where regions of porous media exist in contact with regions of viscous fluid, it is inappropriate to assume that fluid stress is negligible throughout the whole domain. By maintaining the term σ_f , we leverage the machinery of the IB method to treat this scenario in a single unified framework.

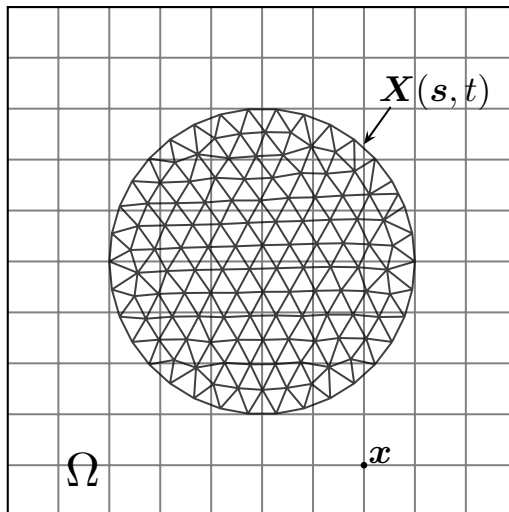


Figure 1: The Lagrangian and Eulerian coordinate systems. Ω indicates the Eulerian domain with coordinate \mathbf{x} . $\mathbf{X}(\mathbf{s}, t)$ represents the current location of the Lagrangian variables with coordinate \mathbf{s} . The Eulerian domain is discretized with a structured grid while an unstructured grid is used to discretized the Lagrangian domain.

Because the aim of this work is to simulate poroelastic cytoskeleton, and the volume fraction of the cytoskeletal network is negligible in comparison to the fluid phase [24], we consider the case when $\phi \ll 1$. Under the assumption of vanishing network volume fraction, (1) - (3) simplify to

$$\mu \Delta \mathbf{u}_f - \nabla p + \xi (\mathbf{u}_n - \mathbf{u}_f) = 0 \quad (7)$$

$$\nabla \cdot \sigma_e + \xi (\mathbf{u}_f - \mathbf{u}_n) = 0 \quad (8)$$

$$\nabla \cdot \mathbf{u}_f = 0, \quad (9)$$

where the last equation enforces the incompressibility of the fluid and comes from (3) under the assumption of vanishing network volume fraction.

2.1. Immersed Boundary Formulation

A natural way of representing the time evolution of a deforming elastic structure is with a moving Lagrangian coordinate system, while fluid variables are more naturally represented with a fixed Eulerian coordinate system. We use the convention that capitalized letters represent Lagrangian variables and lower case letters indicate Eulerian variables. Figure 1 illustrates a typical coordinate system and its discretization.

The communication between the two coordinates is achieved by the spreading operator \mathcal{S} and interpolation operator \mathcal{S}^* . The spreading operator that maps Lagrangian variables to Eulerian variables is

$$\mathbf{f} = \mathcal{S} \mathbf{F} = \int_{\Gamma} \mathbf{F}(\mathbf{s}, t) \delta(\mathbf{x} - \mathbf{X}(\mathbf{s}, t)) d\mathbf{s}, \quad (10)$$

where $\mathbf{s} \in \Gamma$ is the material coordinate and $\mathbf{X}(\mathbf{s}, t)$ denotes the physical position of material point \mathbf{s} at time t . The interpolation operator is given by

$$\mathbf{U} = \mathcal{S}^* \mathbf{u} = \int_{\Omega} \mathbf{u}(\mathbf{x}, t) \delta(\mathbf{x} - \mathbf{X}(\mathbf{s}, t)) d\mathbf{x}, \quad (11)$$

where Ω represents the fluid domain.

For a Lagrangian description of the network, equations (7)–(9) can be rewritten as

$$\mu \Delta \mathbf{u}_f - \nabla p + \mathbf{f}_{\text{drag}}^{\text{net}} = 0 \quad (12)$$

$$\mathbf{F}_{\text{elastic}}^{\text{net}} + \mathbf{F}_{\text{drag}}^{\text{net}} = 0 \quad (13)$$

$$\nabla \cdot \mathbf{u}_f = 0, \quad (14)$$

where $\mathbf{F}_{\text{elastic}}^{\text{net}}$ is the elastic force density expressed in the Lagrangian coordinate system. The Lagrangian drag force density on the network due to the fluid is

$$\mathbf{F}_{\text{drag}}^{\text{net}} = \xi (\mathcal{S}^* \mathbf{u}_f - \mathbf{U}_n). \quad (15)$$

The drag force density on the fluid is equal and opposite to the drag force density on the network and is given by,

$$\mathbf{f}_{\text{drag}}^{\text{net}} = -\xi \mathcal{S} (\mathcal{S}^* \mathbf{u}_f - \mathbf{U}_n). \quad (16)$$

From (13), the structure moves as follows,

$$\frac{\partial \mathbf{X}}{\partial t} = \mathbf{U}_n = \frac{1}{\xi} \mathbf{F}_{\text{elastic}}^{\text{net}} + \mathcal{S}^* \mathbf{u}_f. \quad (17)$$

Given a set of elastic forces, the evolution of the elastic network specified in (17) in conjunction with the viscous flow equations in (12) and (14) are sufficient to determine the dynamics of the fluid-structure system.

At this point, a constitutive law must be specified to compute the elastic force in (13). We consider hyperelastic materials which are characterized by a strain energy density $W = W(\mathcal{A})$ where \mathcal{A} is the network deformation gradient tensor [25, 26]. For such materials, we can describe the Lagrangian elastic force by

$$\widehat{\mathbf{F}}(\mathbf{s}, t)^1 = -\frac{\delta E}{\delta \mathbf{X}}, \quad (18)$$

where E is the total energy of the system,

$$E = \int_{\Gamma} W d\mathbf{s}. \quad (19)$$

¹We use the following notation to differentiate between force density, \mathbf{F} , and force, $\widehat{\mathbf{F}}$.

The material properties of the hyperelastic solid are specified by a constitutive law for the strain energy density. For example, the strain energy density of compressible neo-Hookean elastic solid [25] is

$$W(\mathcal{A}) = \frac{\mu_E}{2} \left(\frac{\text{tr}(\mathcal{A}\mathcal{A}^T)}{J^{2/n}} - n \right) + \frac{\kappa_E}{2} (J - 1)^2, \quad (20)$$

where μ_E denotes the elastic shear modulus, $\kappa_E = 2\mu_E/n + \lambda_E$ is the elastic bulk modulus, λ_E is the second Lamé constant, and n represents the spatial dimension of the problem. $J = \det \mathcal{A}$ is the determinant of the deformation gradient tensor. First studied in the context of rubber elasticity, the neo-Hookean material is an extension of Hooke's law for the case of large deformations. In the approximation of small deformation, the strain $\mathcal{E} = 1/2 (\mathcal{A} + \mathcal{A}^T) - \mathcal{I}$ can be approximated by $\mathcal{E} \approx 1/2 (\nabla \mathbf{q} + \nabla \mathbf{q}^T)$ where \mathbf{q} is the displacement. Under this assumption, (20) simplifies to yield the strain energy density in the regime of linear elasticity

$$W(\mathcal{E}) = \mu_E \text{tr}(\mathcal{E}^2) + \frac{\lambda_E}{2} \text{tr}^2(\mathcal{E}). \quad (21)$$

In the next sections we present two formulations for computing elastic forces based on the variational derivative of the total energy as described in (18). In Section 2.2, the linear approximation in (21) is used to identify the correspondence between elastic moduli and spring stiffness coefficients in a spring-based model of elasticity. In Section 2.3, the strain energy function is used directly to compute the elastic forces in the energy-based model of elasticity.

2.2. Spring model of elasticity

One approach for modeling the elastic network is to represent it by discrete material points connected by elastic springs. Representing Lagrangian mechanics via a network of springs is common in immersed boundary applications [27] and is reminiscent of ideas from Lattice-Spring Models (LSMs) [28, 29]. Due to the fact that ruptures can be simply captured by breaking elastic links (or setting parameters to zero locally), the use of LSMs has traditionally been popular in studies of fracture in solid mechanics [30–33]. However, a known limitation of LSM stems from the fact that nodes are connected with standard springs. Because of this, only a one parameter family of elastic solids with a fixed Poisson ratio can be modeled. Choosing μ_E or λ_E in Eq. (21) dictates the other based on network topology. This limitation can be removed through several methods, including the introduction of bending springs or shear springs connecting material points, but care must be taken to maintain rotational invariance of the model [34, 35]. A relatively recent literature review of LSMs can be found in [28]. The stiffness coefficients and the resting lengths of these springs can be related to the elastic moduli of an isotropic linear elastic material by comparing the discrete and continuous strain energies. Such calculations for linear elastic materials discretized with regular square and triangular lattices can be found in [28].

Because our goal is to model elasticity in cells with arbitrary geometries, we extend this idea to unstructured meshes. A special meshing procedure must be used to guarantee isotropy of the elastic material. We use the Distmesh algorithm because it generates unstructured meshes where the side length of the triangular elements is almost equal [36]. To compute a triangulation, the algorithm assumes the points are connected by springs with repulsive forces. An iterative procedure for minimizing the associated energy generates a set of points that are triangulated by a Delaunay algorithm. The result of this equilibration process is a spring network that approximates an isotropic material.

Discretization of the model

We model the elastic structure as a collection of linear elastic springs with stiffness coefficients k_{ij} and resting lengths $d\ell_{ij}$. The strain energy in the elastic link connecting \mathbf{X}_i to \mathbf{X}_j is given by

$$e_{ij} = \frac{k_{ij} d\ell_{ij}}{2} \left(\frac{|\mathbf{X}_i - \mathbf{X}_j| - d\ell_{ij}}{d\ell_{ij}} \right)^2. \quad (22)$$

The total elastic energy at a point \mathbf{X}_i is

$$E_i = \frac{1}{2} \sum_j e_{ij}, \quad (23)$$

where the sum is understood to be over all j such that \mathbf{X}_j is connected to \mathbf{X}_i . The force exerted by the single elastic spring connecting nodes \mathbf{X}_i and \mathbf{X}_j is

$$-\frac{\partial e_{ij}}{\partial \mathbf{X}_i} = -k_{ij} \left(\frac{|\mathbf{X}_i - \mathbf{X}_j| - d\ell_{ij}}{d\ell_{ij}} \right) \frac{\mathbf{X}_i - \mathbf{X}_j}{|\mathbf{X}_i - \mathbf{X}_j|}, \quad (24)$$

and thus the total force at a point \mathbf{X}_i is

$$\hat{\mathbf{F}}_i = \frac{1}{2} \sum_j -\frac{\partial e_{ij}}{\partial \mathbf{X}_i} = -\frac{\partial E_i}{\partial \mathbf{X}_i}. \quad (25)$$

The force density at \mathbf{X}_i is given by

$$\mathbf{F}_i = \frac{\hat{\mathbf{F}}_i}{dA_i}, \quad (26)$$

where the area weight dA_i at each point \mathbf{X}_i is the sum of one third the area of each triangle with vertex \mathbf{X}_i .

The spring constant k_{ij} is chosen so that the discrete strain energy density from the lattice-spring-like model is consistent with the continuous strain energy density for linear elasticity (21),

$$k_{ij} = \frac{8\lambda_E}{3 d\ell_{ij}} \left(\frac{dA_i + dA_j}{2} \right). \quad (27)$$

A detailed derivation of the above formula can be found in Appendix A. Note that this expression assumes a 2-D elastic material, but an analogous formula can be derived for 3-D.

2.3. Energy-based model of elasticity

A more general approach to describing elastic structures is by directly computing the elastic force from energy functionals. Several methods employ a nodal finite element (FE) mechanics model in the conventional IB method [8, 9] and a generalized IB method, where FE methods are used for both fluid and structure mechanics [37, 38]. In this section, we will rely on the energy functional-based version of the IB method proposed in [9].

Elastic forces are computed through a variational derivative of the energy and without the direct use of stress tensors as in (18). Unlike the spring model, this is a general framework for describing the elasticity of hyperelastic materials that is not restricted to elastic solids with a single family of elastic moduli ($\lambda_E = \mu_E$). An important feature of this elasticity model is that it does not require an isotropic mesh, and thus it can benefit from the computational speed-up of adaptive meshing.

Discretization of the model

In this section we assume a two-dimensional material subjected to planar deformations, but the model is not limited to this case. Given the reference configuration of a material, the structure is discretized into a triangular mesh. For a given triangular element T , the positions of the vertices in reference configuration are denoted by $\mathbf{s}^{(0)}$, $\mathbf{s}^{(1)}$, and $\mathbf{s}^{(2)}$ whereas in the deformed configuration they are $\mathbf{X}^{(0)}$, $\mathbf{X}^{(1)}$, and $\mathbf{X}^{(2)}$ as shown in Figure 2. The set of vectors that describe the deformed and undeformed triangular elastic sheets are $\widetilde{\mathbf{X}}^{(i)} = \mathbf{X}^{(i)} - \mathbf{X}^{(0)}$ and respectively, $\widetilde{\mathbf{s}}^{(i)} = \mathbf{s}^{(i)} - \mathbf{s}^{(0)}$ for $i = 1, 2$. Assuming a linear deformation, the deformed triangular element is given by the following mapping,

$$\left(\widetilde{\mathbf{X}}^{(1)} \quad \widetilde{\mathbf{X}}^{(2)} \right) = \mathcal{A} \left(\widetilde{\mathbf{s}}^{(1)} \quad \widetilde{\mathbf{s}}^{(2)} \right), \quad (28)$$

where \mathcal{A} is the deformation gradient.

It is assumed that the deformation map $\mathbf{X}(\mathbf{s}, t)$ is piecewise function that is linear on each triangle T . Thus the deformation gradient tensor, $\mathcal{A}_{ij} = \partial \mathbf{X}_i / \partial \mathbf{s}_j$, and the strain energy density are constant on each triangle. Therefore the total energy in (18) becomes

$$E = \sum_{T \in \mathcal{T}} W(\mathcal{A}) dA_0(T), \quad (29)$$

where $dA_0(T)$ denotes the area of a triangular element in the reference configuration. \mathcal{T} denotes the entire set of triangular elements in the triangular mesh. We take $\widehat{\mathbf{F}}^{(k)}$ as the force (not force density) at the k th vertex. Starting with (18) and following the derivation in [9] the force at vertex k contributed by triangle T is given by

$$\widehat{\mathbf{F}}_T^{(k)} = - \sum_{i,j=1}^2 \frac{\partial W}{\partial \mathcal{A}_{ij}} \frac{\partial \mathcal{A}_{ij}}{\partial \mathbf{X}^{(k)}} dA_0(T), \quad (30)$$

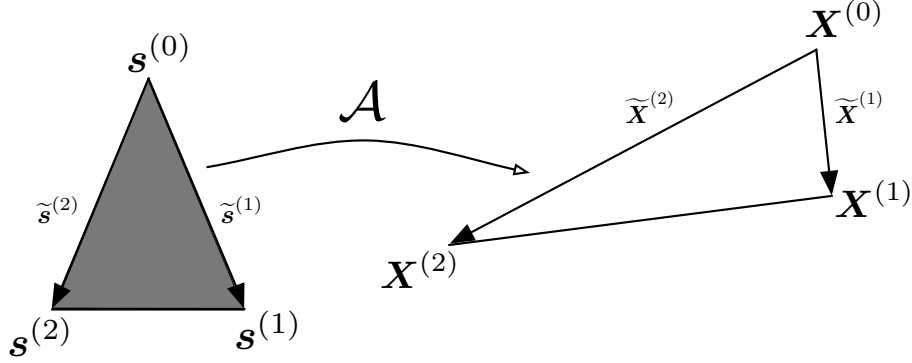


Figure 2: The deformation gradient tensor \mathcal{A} maps the vertices of the undeformed (reference) triangle, $\mathbf{s}^{(i)}$, to the vertices of the deformed triangle given by $\mathbf{X}^{(i)}$ for $i = 0, 1, 2$.

To find the total force at vertex k ,

$$\hat{\mathbf{F}}^{(k)} = \sum_{\mathbf{T} \in \mathcal{T}_k} \hat{\mathbf{F}}_{\mathbf{T}}^{(k)}, \quad (31)$$

where \mathcal{T}_k denotes the set of triangular elements that contain vertex k . To calculate the force density at each point we divide by the characteristic area as in (26).

To illustrate how this method works we consider a compressible neo-Hookean solid under some given deformation. For a set of reference coordinates and a deformed position of the material, the deformation gradient on each triangle is

$$\mathcal{A} = \begin{pmatrix} \tilde{\mathbf{X}}^{(1)} & \tilde{\mathbf{X}}^{(2)} \end{pmatrix} \begin{pmatrix} \tilde{\mathbf{s}}^{(1)} & \tilde{\mathbf{s}}^{(2)} \end{pmatrix}^{-1}. \quad (32)$$

Note that the derivatives of the deformation gradient that appear in (30),

$$\frac{\partial \mathcal{A}_{ij}}{\partial \mathbf{X}^{(k)}} = \begin{pmatrix} \tilde{\mathbf{s}}^{(1)} & \tilde{\mathbf{s}}^{(2)} \end{pmatrix}^{-1}, \quad (33)$$

depend only on the reference configuration and therefore can be pre-computed once per reference mesh configuration. For a compressible neo-Hookean material the strain energy density is given by (20). We recall $J = \det \mathcal{A}$ and compute the first term in the force in (30) by

$$\frac{\partial W}{\partial \mathcal{A}_{ij}} = \mu_E \left(\frac{\mathcal{A}_{ij}}{J} - \frac{\text{tr}(\mathcal{A}\mathcal{A}^T)\mathcal{A}_{ij}^{-T}}{2J} \right) + \kappa_E(J-1)J\mathcal{A}_{ij}^{-T} \quad (34)$$

We note that this formulation for the elastic force is not restricted to a particular model of hyperelasticity. In fact, only the term $\partial W / \partial \mathcal{A}_{ij}$ changes as the material model changes, and it is easy to switch from one material model to another by

changing the strain energy density. In summary, the elastic force is computed as follows

1. Given the reference coordinates of the material, pre-compute the reference area of each triangular element and $\partial\mathcal{A}_{ij}/\partial\mathbf{X}^{(k)}$ for vertex.
2. Given a current position of the material, $\mathbf{X}(\mathbf{s}, t)$:
 - Compute \mathcal{A} and $\partial W/\partial\mathcal{A}_{ij}$ for each triangular element.
 - Compute the elastic force as given in (30) - (31).

2.4. Time Stepping

The drag force on the fluid is equal and opposite to the drag force on the structure, and from Eq. (13) the drag force density on the structure can be replaced by the negative of its elastic force density. Thus,

$$\mathbf{f}_{\text{drag}}^{\text{net}} = -\mathcal{S}\mathbf{F}_{\text{drag}}^{\text{net}} = \mathcal{S}\mathbf{F}_{\text{elastic}}^{\text{net}}, \quad (35)$$

and Eq. (12) can be replaced by

$$\Delta\mathbf{u}_f - \nabla p + \mathcal{S}\mathbf{F}_{\text{elastic}}^{\text{net}} = 0. \quad (36)$$

This rearrangement has the advantage that fast Stokes solvers can be used to find the fluid velocity for given elastic forces. After finding the fluid velocity, the new structure position is updated using Eq. (17). This fractional stepping approach allows the fluid and structure updates to proceed sequentially. Given the current position of the structure, the system is advanced in time as follows:

1. Using either method, compute elastic forces based on the current structure configuration, $\mathbf{X}^n = \mathbf{X}(\mathbf{s}, t^n)$.
2. Spread the force densities onto nearby Eulerian points using Eq. (10).
3. Solve the forced Stokes equations to obtain the fluid velocity \mathbf{u}_f .
4. Interpolate the fluid velocity to the structure using Eq. (11) to obtain \mathbf{U}_f .
5. Compute the structure velocity by Eq. (17) and update the structure by

$$\mathbf{X}^{n+1} = \mathbf{X}^n + \Delta t \left(\frac{1}{\xi} \mathbf{F}_{\text{elastic}}^{\text{net}} + \mathbf{U}_f \right). \quad (37)$$

For the simulations presented in this manuscript, we use periodic boundary conditions on the Eulerian domain and a Fourier-spectral method to solve the Stokes equations. For spreading and interpolation, we use Peskin's approximate δ function with $h = \Delta x = \Delta y$ and $\delta_h(\mathbf{x}) = \delta_h(x)\delta_h(y)$ [27].

3. Numerical Validation

In this section, we validate our IB formulation of poroelasticity with both the spring and energy-based elasticity models by comparing to the continuum equations for a linearly elastic structure. In the limit of small deformations, the nonlinear models presented in this manuscript can be approximated by a linear elastic model.

We consider a test problem in which a circular elastic structure of radius R is expanded uniformly in the radial direction. In this case, the fluid velocity is zero, and the system (7)-(9) simplifies to the single equation

$$\nabla \cdot \sigma_e - \xi \mathbf{u}_n = 0. \quad (38)$$

An isotropic linearly elastic material obeys the following constitutive law:

$$\sigma_e = 2\mu_E \mathcal{E} + \lambda_E \text{tr}(\mathcal{E})\mathcal{I}, \quad (39)$$

where the linearized strain tensor is $\mathcal{E} = 1/2 (\nabla \mathbf{q} + \nabla \mathbf{q}^T)$ and \mathbf{q} denotes displacement. Note that the displacement and velocity are related by

$$\frac{\partial \mathbf{q}}{\partial t} = \mathbf{u}_n. \quad (40)$$

Let q be the radial component of displacement. We obtain a dynamic equation for q by combining equations (38)-(40):

$$\xi q_t = (2\mu_E + \lambda_E) \left(\frac{\partial^2 q}{\partial r^2} + \frac{1}{r} \frac{\partial q}{\partial r} - \frac{q}{r^2} \right). \quad (41)$$

Because there is no external loading on the boundary in this test problem, we take a no-stress boundary condition which has the form

$$\left((2\mu_E + \lambda_E) \frac{\partial q}{\partial r} + \lambda_E \frac{q}{r} \right) \Big|_{r=R} = 0. \quad (42)$$

To test the IB poroelastic method, we compare a refined 1D numerical solution of Eqs. (41) and (42) to a full 2D IB method simulation, where elasticity is computed with both the spring and energy-based models. Specifically, we solve Eqs. (41) and (42) on a 1D cell-centered grid $r \in [\Delta r/2, R - \Delta r/2]$ by discretizing with second order accurate finite difference stencils in space and backward Euler's method in time. We use space and time steps ($\Delta r = R/500$ and $\Delta t = 1e-5$) that are much smaller than those used in the IB calculations. For the tests in this section, we set $\tilde{\lambda}_E = \tilde{\mu}_E = 0.05$, $\tilde{R} = 0.3$, $\tilde{\xi} = 1$, $\tilde{\mu} = 1$, and $\tilde{t} \in [0, 0.5]$, where the tilde indicates dimensionless variables. The radial displacement is initialized to

$$q(r, 0) = 10^{-4} r, \quad (43)$$

which corresponds to a uniform expansion of the disk 0.01% in the radial direction. With these parameters, the characteristic timescale for relaxation is

approximately 0.14 dimensionless time units (this can be found by computing the first eigenvalue of the solution via separation of variables). The radial component of the displacement $q(r, t)$ at several time values is shown in Fig. 3.

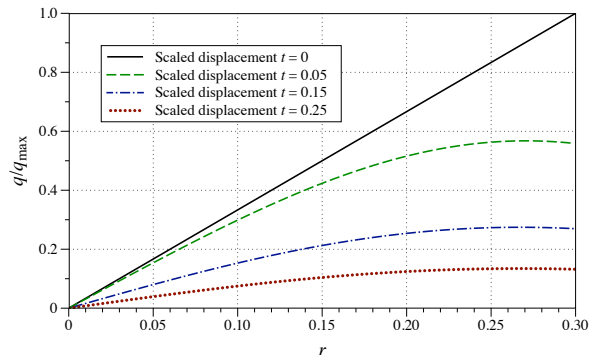


Figure 3: Displacement $q(r, t)$ in the radial direction at several time points divided by the maximum displacement $3.0e-5$.

For the IB simulations, the fluid domain is $[0, 1] \times [0, 1]$ with periodic boundary conditions. The domain is discretized using N grid points in each direction so that $\Delta x = \Delta y = 1/N$. The Lagrangian domain is a circle of radius 0.3 that is triangulated using Distmesh [36]. For a 64×64 Eulerian grid, the Lagrangian grid consists of 3285 points with an average length of a triangle edge (Δs) approximately equal to the Eulerian grid spacing Δx . Both grids are refined to maintain the same relative resolution. For the energy-based model, we use the strain energy function for a neo-Hookean material. One could use linear elasticity in the energy-based model given the small strain in this test. However, as demonstrated in Appendix B, linear elasticity leads to unbalanced torques and unphysical rotation of the material. Nonlinear constitutive laws are not more difficult to use in this formulation, and they ensure that the torques balance discretely.

To estimate the error in the IB simulations, we treat the refined finite difference solution as the exact solution. The displacement from the finite difference solution is interpolated to the points on the Lagrangian grid to compare the two solutions. Convergence data for both the spring and energy-based models are summarized in Figs. 4 and 5. Fig. 4 shows the L_∞ and L_2 norm of the difference between the refined finite difference radial displacement and the computed IB displacement normalized by maximum displacement over time for several grid refinements. The error appears to decrease linearly in time. Fig. 5 shows the error at $t = 0.1$ at different grid refinements and a power function fit to the data. The spring model converges in space and time with a rate slightly less than one, whereas the energy-based model converges with a rate slightly higher than one (compare the exponents of the power function fits in Fig. 5(a) to 5(b)).

In addition to having a slightly higher convergence rate, the relative errors in the energy-based model are approximately an order of magnitude smaller than those in the spring model (compare the scales on Fig. 4(a) to that of Fig. 4(c)).

4. Applications

In this section, the modeling framework described previously is applied to two different cellular systems: blebbing and amoeboid cell crawling. Intracellular fluid flow and cytoplasmic mechanics are important in both applications, and we demonstrate that a poroelastic model of the cytoplasm is necessary to reproduce the relevant cell behavior.

4.1. Cellular blebbing

Blebs are spherical membrane protrusions characterized by a separation of the cell membrane from the cytoskeleton. The cell cortex is the specialized layer of the cytoskeleton adjacent to the membrane composed primarily of actin filaments. The cortex is under tension due to molecular motor activity on the actin, and it is linked to the membrane by specialized proteins. A bleb is nucleated when there is a local disruption in these attachment proteins, for example due to local a increase in cortical tension. Blebs have been observed in several migrating cell types [39, 40], and it has been hypothesized that blebbing

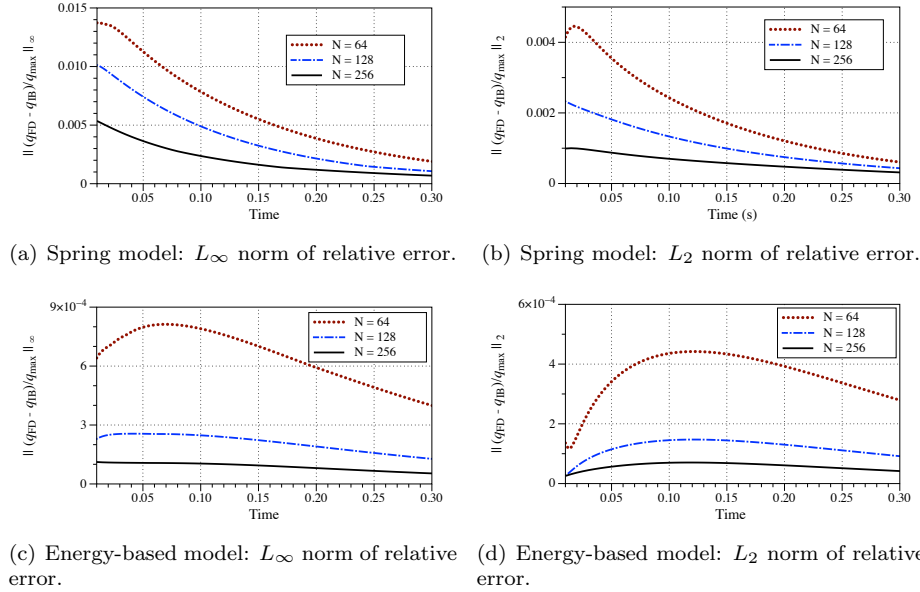
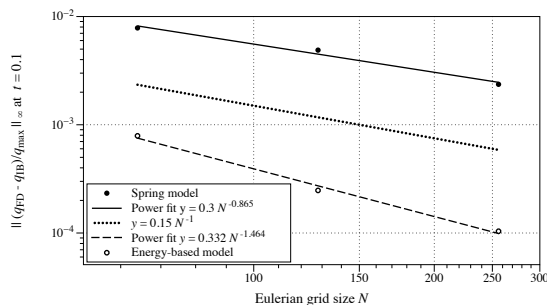
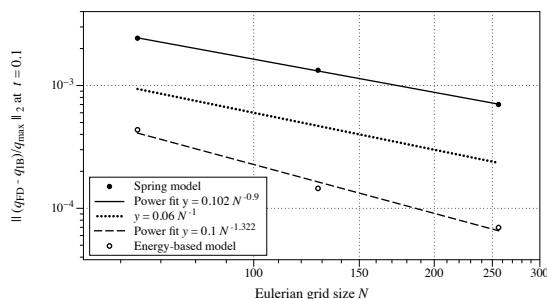


Figure 4: Norm of the difference between the refined finite difference solution $q(r, t)_{FD}$ and $q(r, t)_{IB}$ over time scaled by maximum displacement.



(a) L_∞ norm of scaled error at $t = 0.1$.



(b) L_2 norm of scaled error at $t = 0.1$.

Figure 5: Norm of the difference between the refined finite difference solution $q(r, t)_{FD}$ and $q(r, t)_{IB}$ scaled by maximum displacement at $t = 0.1$.

is involved in amoeboid cell motility [18]. Motile cancer cells treated with anti-tumor treatments switch migration modes from a mesenchymal mode, driven by actin polymerization at the leading edge of the cell, to an amoeboid mode, driven by intracellular pressure and cytoplasmic steaming [41].

Recent experimental results have led to conflicting hypotheses about pressure propagation in the cell. In [10], the authors treated part of a blebbing cell with a drug to locally inhibit actin polymerization. Blebbing ceased in the drug treated area, and continued in the untreated area. The authors concluded that pressure equilibration is slow compared to the timescale of bleb expansion, and they argued that the poroelastic properties of the cytoplasm are responsible for the slower pressure equilibration. In another study, a bleb was nucleated by ablating the cortex with a laser [19]. A second bleb was nucleated a few seconds after the first bleb at various distances from the first nucleation site. The second bleb was the same size regardless of where it was nucleated. The authors concluded from this experiment that intracellular pressure equilibrates quickly compared to the timescale of bleb expansion. Because it is impossible to measure experimentally the spatial distribution of intracellular pressure, mathematical modeling can be used as a tool to understand how pressure is propagated in a blebbing cell. With

this goal in mind, we compare two mechanical models of the cytoplasm: viscous fluid and poroelastic material.

4.1.1. Viscous cytoplasm model

In [42], we presented a model of a blebbing cell in which the cytoplasm was modeled as a viscous fluid. The cell membrane was modeled as an impermeable elastic structure that moves with the fluid velocity, and the actin cortex was modeled as a one-dimensional poroelastic structure attached to the membrane. The force balance equation for the fluid phase includes terms from the elastic membrane, the cortex/membrane attachment, as well as the drag with cortex:

$$\mu\Delta\mathbf{u} - \nabla p + \mathbf{f}_{\text{elastic}}^{\text{mem}} + \mathbf{f}_{\text{attach}}^{\text{mem/cortex}} + \mathbf{f}_{\text{drag}}^{\text{cortex}} = \mathbf{0} \quad (44)$$

$$\nabla \cdot \mathbf{u} = 0. \quad (45)$$

On the cortex, the drag force is balanced by elastic forces within the cortex and attachments with the membrane:

$$\mathbf{F}_{\text{drag}}^{\text{cortex}} + \mathbf{F}_{\text{elastic}}^{\text{cortex}} + \mathbf{F}_{\text{attach}}^{\text{cortex}} = \mathbf{0}. \quad (46)$$

For the Lagrangian force densities, we use the convention that the subscript describes the type of force and the superscript describes the structure acted upon by the force. Expressions for these forces are described below.

Similar to (15), the drag force density from the cortex moving through the fluid is given by

$$\mathbf{F}_{\text{drag}}^{\text{cortex}} = \zeta (\mathcal{S}^* \mathbf{u} - \mathbf{U}_{\text{cortex}}), \quad (47)$$

and the drag force density on the fluid is related to the cortex drag force density by

$$\mathbf{f}_{\text{drag}}^{\text{cortex}} = -\mathcal{S} \mathbf{F}_{\text{drag}}^{\text{cortex}}. \quad (48)$$

The Lagrangian elastic force densities on the membrane and cortex are computed by

$$\mathbf{F}_{\text{elastic}}^i = \frac{\partial}{\partial s} (T_i \boldsymbol{\tau}_i), \quad (49)$$

where T_i is tension and $\boldsymbol{\tau}_i$ is the tangent vector to the curve $\Gamma_i = \mathbf{X}_i(s, t) = \mathbf{X}_{\text{mem}}(s, t)$ or $\mathbf{X}_{\text{cortex}}(s, t)$. In reference arc length coordinates, tension is given by

$$T_i = \gamma_i + k_i \left(\left| \frac{\partial \mathbf{X}_i}{\partial s} \right| - 1 \right), \quad (50)$$

which describes an elastic material with stiffness k_i with an additional resting tension γ_i . Membrane-cortex attachment is modeled by elastic springs attaching the membrane to the cortex with a force density given by

$$\mathbf{F}_{\text{attach}}^{\text{mem/cortex}} = k_{\text{attach}} \left(|\mathbf{X}_{\text{mem}} - \mathbf{X}_{\text{cortex}}| \right) \frac{\mathbf{X}_{\text{mem}} - \mathbf{X}_{\text{cortex}}}{|\mathbf{X}_{\text{mem}} - \mathbf{X}_{\text{cortex}}|}. \quad (51)$$

Given a configuration of the membrane and cortex, the forces are computed, and the velocities of the fluid and cortex are obtained by solving Eqs. (44)-(46)

as described in Section 2.4. Then, the positions of the membrane and cortex are updated with their respective velocities,

$$\frac{d\mathbf{X}_{\text{mem}}}{dt} = \mathcal{S}^* \mathbf{u} = \mathbf{U}, \quad (52)$$

$$\frac{d\mathbf{X}_{\text{cortex}}}{dt} = \frac{1}{\zeta} \left(\mathbf{F}_{\text{elastic}}^{\text{cortex}} + \mathbf{F}_{\text{attach}}^{\text{cortex/mem}} \right) + \mathbf{U} = \mathbf{U}_{\text{cortex}}. \quad (53)$$

4.1.2. Poroelastic cytoplasm model

The model formulation is the same as above with the addition of a poroelastic cytoskeletal network in the cell interior (see Fig. 6). The fluid equations have

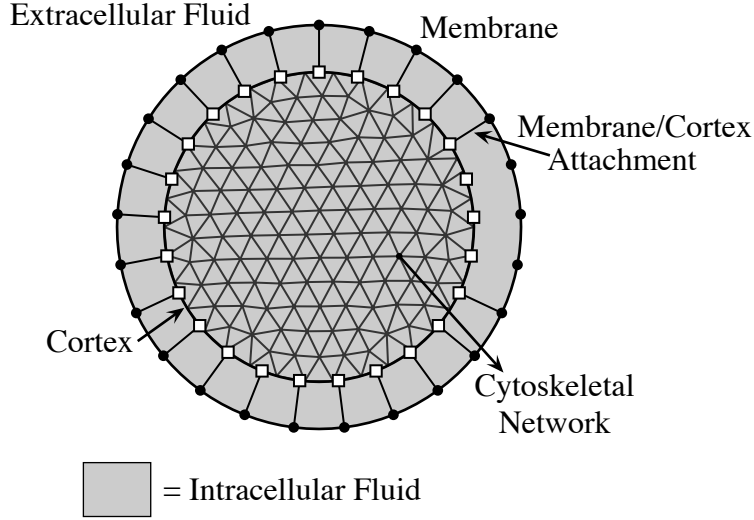


Figure 6: Bleb Model schematic. A bleb is initiated by removing adhesive links between the membrane and the cortex.

an additional term for cytoskeletal drag,

$$\mu \Delta \mathbf{u} - \nabla p + \mathbf{f}_{\text{elastic}}^{\text{mem}} + \mathbf{f}_{\text{attach}}^{\text{mem/cortex}} + \mathbf{f}_{\text{drag}}^{\text{cortex}} + \mathbf{f}_{\text{drag}}^{\text{net}} = \mathbf{0} \quad (54)$$

$$\nabla \cdot \mathbf{u} = 0.$$

The superscript “net” indicates the cytoskeletal network. The force density balance on the cortex includes an additional attachment term to link the cortex to the cytoskeleton,

$$\mathbf{F}_{\text{drag}}^{\text{cortex}} + \mathbf{F}_{\text{elastic}}^{\text{cortex}} + \mathbf{F}_{\text{attach}}^{\text{cortex/mem}} + \mathbf{F}_{\text{attach}}^{\text{cortex/net}} = \mathbf{0}. \quad (55)$$

Similarly, the force density balance on the cytoskeleton is

$$\mathbf{F}_{\text{drag}}^{\text{net}} + \mathbf{F}_{\text{elastic}}^{\text{net}} + \mathbf{F}_{\text{attach}}^{\text{net/cortex}} = \mathbf{0}, \quad (56)$$

where cytoskeletal drag is defined as

$$\mathbf{F}_{\text{drag}}^{\text{net}} = \xi (\mathbf{U}_{\text{net}} - \mathcal{S}^* \mathbf{u}). \quad (57)$$

The attachment force density on the network is the opposite of the corresponding force density on the cortex, with the proper scaling to ensure that the two forces balance,

$$\int_{\Omega} \left(\mathcal{S} \mathbf{F}_{\text{attach}}^{\text{cortex/net}} + \mathcal{S} \mathbf{F}_{\text{attach}}^{\text{net/cortex}} \right) dx = 0. \quad (58)$$

Elasticity is computed by the spring model of elasticity described in Section 2.2. Each structure moves with its own velocity,

$$\frac{d\mathbf{X}_{\text{mem}}}{dt} = \mathcal{S}^* \mathbf{u} = \mathbf{U}, \quad (59)$$

$$\frac{d\mathbf{X}_{\text{cortex}}}{dt} = \frac{1}{\xi} \left(\mathbf{F}_{\text{elastic}}^{\text{cortex}} + \mathbf{F}_{\text{attach}}^{\text{cortex/mem}} + \mathbf{F}_{\text{attach}}^{\text{cortex/net}} \right) + \mathbf{U} = \mathbf{U}_{\text{cortex}}, \quad (60)$$

$$\frac{d\mathbf{X}_{\text{net}}}{dt} = \frac{1}{\xi} \left(\mathbf{F}_{\text{elastic}}^{\text{net}} + \mathbf{F}_{\text{attach}}^{\text{net/cortex}} \right) + \mathbf{U} = \mathbf{U}_{\text{net}}. \quad (61)$$

4.1.3. Blebbing Simulation

We simulate bleb expansion using both a viscous fluid model and a poroelastic model of cytoplasm to compare intracellular pressure propagation in each case. An Eulerian grid of size 64×64 on the domain $[0, 30] \mu\text{m} \times [0, 30] \mu\text{m}$ was used. The Lagrangian grid was an unstructured mesh with 6710 points (267 on the boundary) discretized by Distmesh [36]. This corresponded to approximately two Lagrangian points per Eulerian grid cell on the boundary.

The action of molecular motors generates tension within the cortex (represented by γ_{cortex} in the model). The cortical tension is transmitted to the membrane via membrane/cortex attachment, which in turn generates a pressure jump across the cell membrane. To initiate a bleb, we remove membrane/cortex attachment in a small area (see Fig. 6). If the membrane is parameterized by $\theta \in [-\pi, \pi)$, we remove attachment in a region where $|\theta| < 11\pi/160$. Cortical tension is not transmitted to the membrane in this region, which leads to a locally reduced pressure. The pressure gradient drives a flow of cytosol to inflate the bleb by expanding the membrane in the region of ruptured adhesion. The bleb eventually stops expanding when membrane tension balances intracellular pressure.

Simulation results are shown in Fig. 7 using model parameters from Table 1 for both simulations. In the simulation with a viscous fluid cytoplasm, the pressure jump across the membrane after the bleb expands is reduced by 8% from its initial value (Fig. 7(a)). In contrast, the pressure jump decreases 27% with a poroelastic cytoplasm (Fig. 7(b)). When the attachment between

Table 1: Bleb Model parameters.

Symbol	Quantity	Value
r_{mem}	Cell radius	10 μm
γ_{mem}	Membrane surface tension	40 pN/ μm
k_{mem}	Membrane stiffness coefficient	4 pN/ μm
r_{cortex}	Cortex radius	9.99 μm
γ_{cortex}	Cortical tension	250 pN/ μm
k_{cortex}	Cortical stiffness coefficient	100 pN/ μm
λ_E	Cytoskeletal shear modulus	1 kPa
$k_{\text{attach}}^{\text{cortex/mem}}$	Cortex/Membrane attachment stiffness coefficient	2502.5 pN/ μm^3
$k_{\text{attach}}^{\text{mem/cortex}}$	Membrane/cortex attachment stiffness coefficient	2502.0 pN μm^3
$k_{\text{attach}}^{\text{cortex/net}}$	Cortex/cytoskeleton attachment stiffness coefficient	100 pN/ μm^3
$k_{\text{attach}}^{\text{net/cortex}}$	Cytoskeleton/cortex attachment stiffness coefficient	985.5 pN/ μm^4
μ	Cytosolic viscosity	1 Pa-s
ζ	Cortical drag coefficient	10 pN-s/ μm^3
ξ	Cytoskeletal drag coefficient	10 pN-s/ μm^4
L	Fluid computational domain size	30 μm
Δx	Fluid grid step size	$L/64$
Δs	Initial structure grid step size	$2\pi r_{\text{mem}}/267$
Δt	Time step size	5e-5 s

the membrane and cortex is removed, the cortex contracts and compresses the cytoskeleton. This compression generates a restoring elastic force that relieves pressure. The reduced pressure also leads to smaller steady state bleb sizes when all parameters are the same (compare Fig. 7(a) and Fig. 7(b) at $t = 20$ s).

Fig. 8 shows the normalized pressure drop across the cell over time. The pressure drop is defined as the pressure at the front of the cell minus the pressure at the rear of the cell (locations are the black dots illustrated in the last panel of Fig. 7(b)). This value is normalized by the maximum pressure value over time in each simulation. The data show two effects of poroelasticity. (1) There is a time delay when the front half of the cell feels the effects of attachment breaking. The peak pressure occurs almost immediately in the fluid model, while it takes about half a second to occur in the poroelastic model (see inset of Fig. 7(b)). (2) On a longer timescale, pressure equilibrates more slowly across the poroelastic cytoplasm. When the cytoplasm is compressed, there is a timescale for stress to redistribute throughout the elastic network.

In [42], we found the timescale of bleb expansion was dominated by intracellular drag and not fluid viscosity in the fluid model of the cytoplasm. The model predicted a value of the drag coefficient that can only be achieved with a cortical gap size that is an order of magnitude smaller than experimental observations. These results indicate that a viscous fluid model of the cytoplasm is inadequate to study pressure dynamics in blebbing cells.

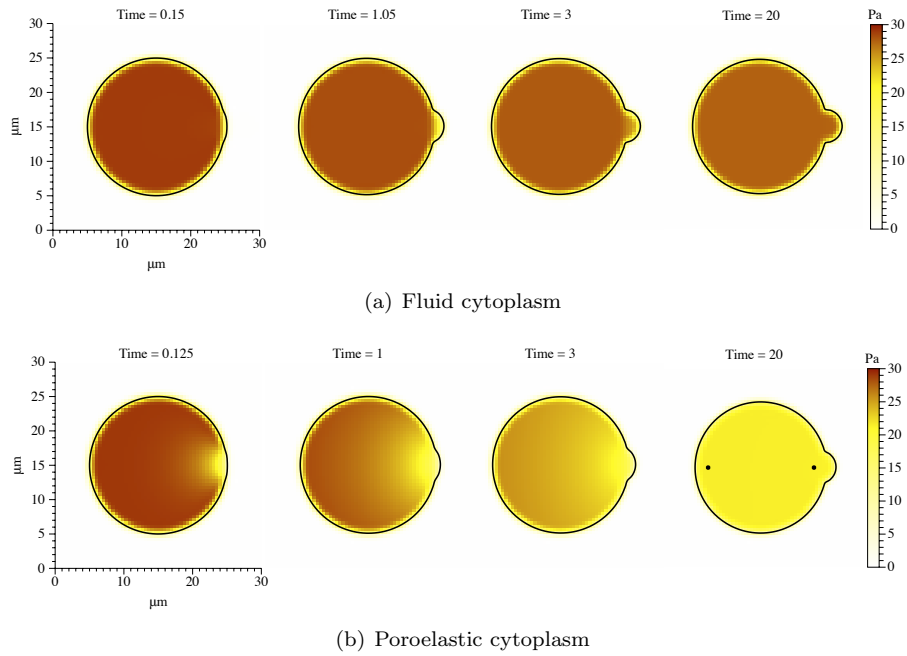


Figure 7: Membrane position and pressure in the bleb model at several time values for both the (a) fluid cytoplasm and (b) poroelastic cytoplasm. In (b) the black dots indicate point locations where pressure values were used to compute the pressure drop across the cell in Fig. 8.

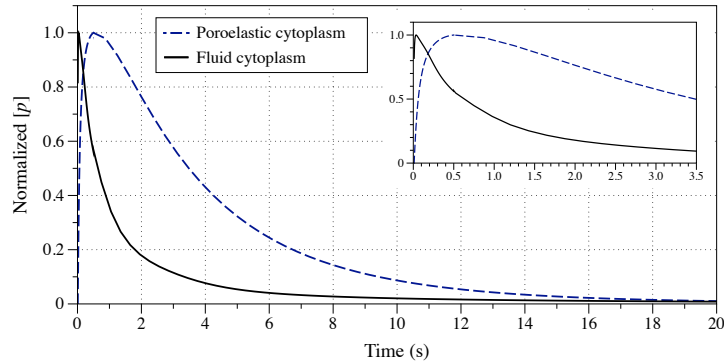


Figure 8: Difference between the pressure at the front of the cell (near the bleb) minus the back of the cell divided by the maximum pressure for each simulation. The inset figure shows the first 3.5 seconds.

The poroelastic cytoplasm model provides the appropriate framework to investigate the effects intracellular pressure propagation and cytoplasmic rheology

on blebbing and cell motility. From Fig. 8, we can see that poroelasticity slows bleb expansion by increased intracellular drag and stress relaxation through the elastic network. We hypothesize that both effects are needed to capture the correct pressure dynamics. We will report a more detailed study of intracellular pressure in blebbing cells in the future.

4.2. Cell crawling

Understanding cell motility is a fundamental problem in modern biology. Cells translocate across a substrate through a complex interaction of chemical and mechanical processes. A large body of modeling work has been dedicated to understanding the mechanics of this process. In the traditional paradigm of cell crawling, the anterior edge of the cell is driven forward by polymerization of the actin network within the cell. The front then adheres to the underlying substrate, the cell contracts, and the posterior is drawn forward [43, 44]. To date, much theoretical work on cell crawling has focused on the dynamics of the actin structure within the cell. However, some motile cells are known to drive the anterior edge forward not with actin polymerization, but with pressure driven flows of cytoplasm [17, 18, 21, 39]. Most models of cell crawling do not account for the effects of viscous flow, or intracellular pressure within the cell. In this context, it is more appropriate to treat the cell interior as a porous, elastic medium permeated with viscous fluid.

Because of its large size and extensive experimental observations [45], *Physarum polycephalum* is an excellent cell for exploring the role of intracellular fluid flow in cell locomotion. Under certain conditions, *Physarum* have been known to translocate while generating periodic anterior/posterior flows of cytoplasm along the centerline of the cell body. In [21], the authors performed spatiotemporal measurements of the cell shape deformation and the intracellular fluid velocity in migrating *Physarum*. These data show that cell deformations and changes in intracellular fluid velocity propagate as coordinated waves along the length of the cell in the direction of migration. Net cellular motion results from the spatiotemporal organization of these oscillating contractions, the flow of cytoplasm, and adhesive interactions with the substrate. Precisely how the coordination of these effects generates cell motility is not understood. Therefore we ask, what role does intracellular fluid play in this form of cell motility? Our modeling framework is well adapted to address this question with minimal alteration to account for substrate interactions. We compare crawling cells with and without the effects of viscous cytosol and show that fluid effects are critical to generating motility in this context.

4.2.1. Constitutive Laws

Physarum specimens are enclosed by a bilipid membrane which is connected to an underlying cortex (comprised largely of cortical actin). The cell interior is comprised of cytoskeleton (filamentous actin, various cross linker proteins, etc.) permeated by cytosol (water, monomeric proteins, organelles, etc.). The cell interacts with the underlying substrate through adhesive complexes which

transmit stresses from the cell’s internal structure to the external surface. As in the previous section, we model the cytosol as a viscous incompressible fluid and the cytoskeleton as a porous elastic network. Because the distance between cell membrane and cortex is small compared to the size of *Physarum* (several hundred microns long), we do not distinguish between the membrane and underlying cortex as in the previous application. The combined membrane and cortex are represented as a single impermeable structure. For brevity, we will refer to this object as the “membrane”. Finally, because cell/substrate interactions are necessary for cell crawling, we introduce a third Lagrangian structure which we refer to as adhesive points to account for adhesive complexes. These adhesive points represent the primary difference between this model of cell crawling and the model of cellular blebbing presented in Section 4.1. See Figure 9 for a diagram of the model cell.

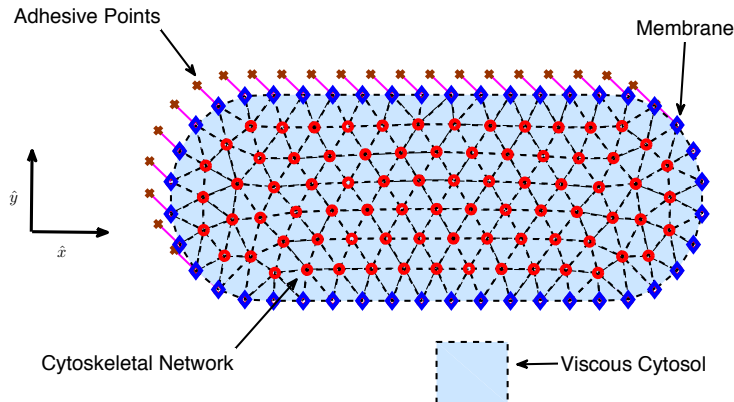


Figure 9: Schematic of our model *Physarum*. Cytoplasmic flow is driven by contraction within the cytoskeletal network.

The elastic properties of the membrane are given by Eqs. (49)-(50), as in the previous section. We again include an interaction force density, however this time the membrane is attached directly to the cytoskeleton. This force density, $\mathbf{F}_{\text{attach}}^{\text{mem/net}}$, takes the form of Hookean springs linking the membrane and the boundary of the cytoskeletal network.

The balance of force densities on the internal cytoskeleton is much the same as in Section 4.1. The elastic forces within the network are calculated using the spring model. The model is also altered to take into account stresses due to adhesion to the substrate underlying the cell. We account for adhesion interactions between the cell and the substrate through the adhesive points. Each network point \mathbf{X}_{net} has an associated adhesive point \mathbf{X}_{adh} , to which it is cou-

pled through a Hookean spring:

$$\mathbf{F}_{\text{adh}}^{\text{net}} = k_{\text{adh}} (\mathbf{X}_{\text{adh}}(\mathbf{s}, t) - \mathbf{X}_{\text{net}}(\mathbf{s}, t)). \quad (62)$$

Finally, we input an active contraction force density ($\mathbf{F}_{\text{active}}^{\text{net}}$) within the network to drive the simulation. Thus, the force density balance on the network becomes

$$\mathbf{F}_{\text{drag}}^{\text{net}} + \mathbf{F}_{\text{active}}^{\text{net}} + \mathbf{F}_{\text{elastic}}^{\text{net}} + \mathbf{F}_{\text{attach}}^{\text{net}/\text{mem}} + \mathbf{F}_{\text{adh}}^{\text{net}} = 0. \quad (63)$$

The coupling of the adhesive points to the cytoskeletal network is balanced by the interaction between the adhesive points and the substrate that the cell is moving across. This substrate interaction is given by

$$\mathbf{F}_{\text{subs}} = -\zeta (\mathbf{X}_{\text{adh}}, t) \frac{\partial \mathbf{X}_{\text{adh}}}{\partial t} = -\zeta (\mathbf{X}_{\text{adh}}, t) \mathbf{U}_{\text{adh}}. \quad (64)$$

Here ζ is a viscous drag coefficient that varies in space and time. Modulation of this function represents the cell adhering more strongly (or weakly) to the substrate.

This completes the balance of force densities on the adhesive points

$$\mathbf{F}_{\text{subs}} - \mathbf{F}_{\text{adh}}^{\text{net}} = 0. \quad (65)$$

4.2.2. Results

We begin by discretizing an elongated domain with semicircular end-caps (see Figure 9). This shape is chosen to represent an idealized *Physarum* cell. The simulation is driven by prescribing the active term in the network force density balance (63) as

$$\mathbf{F}_{\text{active}}^{\text{net}} = \frac{A_{\text{active}}}{2} (\cos(\kappa x_{\text{net}} - \omega t) (\hat{\mathbf{v}}_{ij} \cdot \hat{\mathbf{y}}) + 1) \hat{\mathbf{v}}_{ij}. \quad (66)$$

Here, x_{net} is the reference longitudinal body coordinate of a link within the cytoskeletal network, $\hat{\mathbf{v}}_{ij}$ is the orientation vector of the network link, and $\hat{\mathbf{y}}$ is the unit vector in the lateral direction. This form of active contraction within the network is chosen to mimic the peristaltic waves of contraction witnessed in *Physarum* specimens *in vivo*. Similarly, the drag coefficient in (64) is prescribed as a spatiotemporal wave:

$$\zeta = \frac{A_{\text{adh}}}{2} (\cos(\kappa x_{\text{adh}} - \omega t) + 1) + \varepsilon. \quad (67)$$

The parameter ε represents uncoordinated nonspecific friction between the cell and the substrate.

Simulations of the full model (Eqs. (63)-(65)) are performed using the parameters listed in Table 2. A complimentary simulation is run where all parameters pertaining to the fluid and the cell membrane are set to zero. When $k_{\text{mem}} = \mathbf{u} = k_{\text{connect}} = 0$, the model reduces to simulating an elastic, contractile network moving through a viscous stationary medium and adhering to

Table 2: Model parameters for crawling simulation.

Symbol	Quantity	Value
L_x	Cell length	300 μm
L_y	Cell width	100 μm
γ_{mem}	Membrane surface tension	4 pN/ μm
k_{mem}	Membrane stiffness coefficient	2.5 pN/ μm
λ_E	Cytoskeletal elastic modulus	1.25 kPa
ω^{-1}	Contraction period	100 s
κ^{-1}	Contraction wave length	1200 μm
μ	Cytosolic viscosity	5e-2 Pa-s
ξ	Cytoskeletal drag coefficient	50 pN-s/ μm^4
A_{active}	Strength of active contraction	1.5e4 pN
A_{adh}	Strength of coordinated adhesion	6.25e2 Pa-s/m
ε	Strength of uncoordinated adhesion	15.625 Pa-s/m
L	Fluid computational domain size	400 μm
Δx	Fluid grid step size	$L/64$
Δs	Initial structure grid step size	9.37 μm
Δt	Time step size	1e-5 s

an underlying substrate. We refer to this scenario as an “elastic” cell, while simulation of the full model will be referred to as the “poroelastic” cell.

To analyze the motility of each cell, we calculate the geometric center of the cell as a function of time. A time course of each cell is shown in Figure 10. The migration velocity of the poroelastic cell is approximately equal to that measured in [21]. Notice that the migration velocity of the elastic cell is greatly reduced compared to that of the poroelastic cell. To explain this phenomenon, we examine the stresses that each cell is transmitting to the substrate via the adhesive points.

For each model cell, we calculate the adhesion tension, \mathbf{T}_{subs} , applied to the substrate as an integral of the substrate stress applied to the adhesions:

$$\mathbf{T}_{\text{subs}}(x, t) = \int -\mathbf{F}_{\text{subs}} dy. \quad (68)$$

Generally we are interested in tension applied in the longitudinal direction, as that is the axis of motion for the cell. To this end, we calculate

$$T(x, t) = \mathbf{T}_{\text{subs}} \cdot \hat{\mathbf{x}}. \quad (69)$$

Figure 11 shows kymographs of $|T(x, t)|$ for a representative poroelastic cell, as well as for an elastic cell when all common parameters were kept fixed. Notice that the tension generated (in the direction of motion) by the poroelastic cell is significantly greater than that generated by the simply elastic cell.

The full poroelastic cell generates traction stresses that are approximately an order of magnitude larger than the elastic cell. This explains the drastically different migration speeds seen in Figure 10. The cause of this increase in

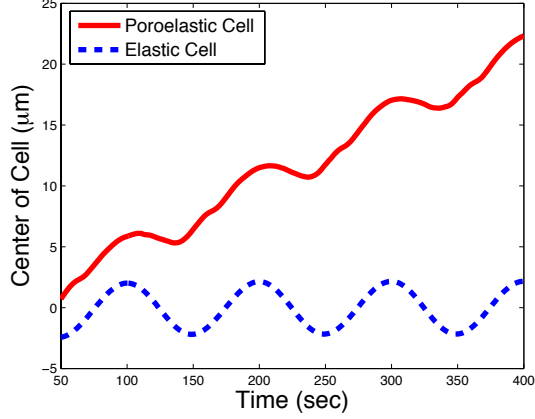


Figure 10: Time course of the centers of model *Phyuysarum* cells.

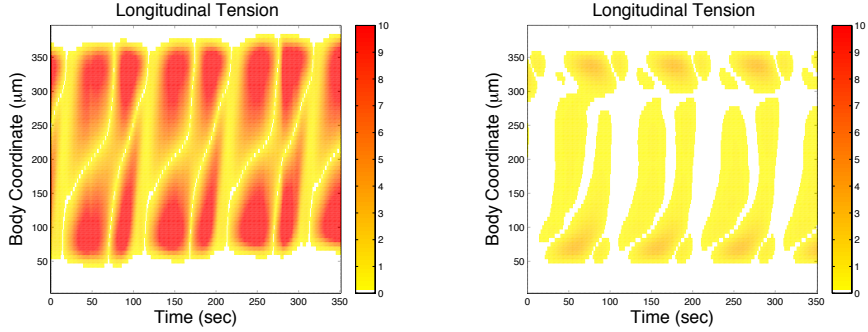


Figure 11: Kymographs of absolute value of traction tension along cell axis. Measurements for a poroelastic cell (including fluid and membrane) are shown on the left. Measurements for an elastic cell are shown on the right. All values have been nondimensionalized by the characteristic tension of crawling with nonspecific adhesion ($\epsilon L^2 \omega$).

traction stresses can be traced back to the incompressibility of the intracellular fluid in the poroelastic cell. In both cells, the cytoskeletal network is being contracted with a *lateral* bias. In the case of the full cell, these laterally preferential contractions cause the incompressible fluid to flow in the *longitudinal* direction. This flow exerts longitudinal drag forces on the network, which are in turn transmitted to the adhesive points and the substrate. In the case of the elastic cell, this does not happen. Contracting the network laterally only causes small longitudinal deformations because the Poisson ratio of the elastic network is nonzero. This is a substantially weaker effect, and thus, longitudinal adhesion stresses are greatly diminished. Therefore, the model indicates that the flow of intracellular fluid is critical in generating cell locomotion from the

type of peristaltic contractions witnessed in *Physarum*.

5. Conclusions

In this manuscript, we presented a novel numerical method for simulating the dynamics of poroelastic materials immersed in a viscous fluid. The method uses the framework of the IB method: quantities associated with the elastic structure are represented in a moving Lagrangian coordinate system and the fluid variables are represented in a fixed Eulerian coordinate system. Implementing our model requires a method for solving the fluid equations along with routines to compute elastic forces and to transfer data between the Lagrangian mesh and the Eulerian grid. Because the structure and the fluid mechanics can be decoupled at each time step, fast methods for solving the equations of the fluid mechanics can be used.

The popularity of the IB and related methods is driven by its simplicity and robustness. The price of this simplicity is the restriction on the largest stable time step permitted by such schemes for stiff structures. The method presented here inherits the time step restriction of IB methods, and the relative motion between the structure and fluid introduces another possible time step restriction. The elastic force directly enters the equation of the motion of the porous structure in Eq. (17). When the drag coefficient between the fluid and structure is small, this additional numerical stiffness may further limit the time step. Implicit-time IB methods overcome the time step restriction and could be used here. However their implementation is much more involved and is a subject of ongoing research [46–52].

We presented two methods for computing elasticity, one based on a network of discrete springs and the other based on the strain energy of hyperelastic materials. Other methods of computing the elastic forces could also be used with our formulation, such as those presented in [7, 8]. Spring models have frequently been used in IB simulations in the past. Our analysis shows how to identify the effective elastic modulus of a network of springs. While spring models are simple, they have several limitations. First it is not clear what constitutive laws are modeled for the large deformations that are common in biological problems. Second, the mechanical properties of the material depend on the structure of the mesh. We used a special discretization procedure to ensure that the material was isotropic. In computational experiments with spring models on other meshes, artifacts of the mesh were apparent. The spring model does not naturally generalize to nonuniform meshes, but this is straightforward with the energy-based method. This is an important consideration when local mesh refinement is required. The energy-based models do not have the limitations of the spring-based model, and in our tests, the energy-based method was much more accurate.

We note that we compared the models with linear elasticity for validation, but both the spring model and the energy-based model involved nonlinear elastic materials. The energy-based method could be used to describe a linearly elastic material. It is important to note that linear elasticity is not frame invariant,

and this approach can result in unbalanced torques and unphysical rotations of the material. In Appendix B we compare linear and nonlinear elasticity for a test problem with large deformation. This test demonstrates the effect of the spurious torques generated with linear elasticity. Nonlinear constitutive laws do not introduce any additional complexity to the method, and they can be used for problems with small and large deformations. This is why we chose a nonlinear model for the tests presented in this paper.

While we considered problems of small length scales where the Reynolds number is zero, extending the method to problems with inertia is straightforward. This work was motivated by problems in cell biology, and our results showed that poroelastic models were essential to describe the dynamics in the systems presented. However, the modeling framework and methods are not limited to applications in cell biology. Porous structures can be found in many contexts in biology and engineering, and our models could be adapted to these problems.

Acknowledgements

This work was supported in part by NSF grant DMS-1160438 to RDG and NSF DMS-1226386 to RDG and WS. Additionally, CAC was supported by NSF grant DSM-1148897.

Appendix A. Relating the Spring Stiffness to Elastic Modulus

In this appendix, we derive expressions that relate the stiffness constants in the spring model to the elastic moduli of an isotropic elastic medium. To derive the expression (27) for the stiffness constant k_{ij} , we compute the discrete strain energy from a pure shear and compressive deformation. We choose k_{ij} to be consistent with the continuous strain energy density of a linear elastic material in the limit of infinitesimal deformation.

Shear Modulus

Consider a shear deformation that maps $(x, y) \rightarrow (x + \gamma y, y)$. The deformation gradient is then

$$\mathcal{A} = \begin{pmatrix} 1 & \gamma \\ 0 & 1 \end{pmatrix}. \quad (\text{A.1})$$

Let $\mathbf{v}_{ij} = \mathbf{X}_i - \mathbf{X}_j$ and let $\hat{\mathbf{v}}_{ij} = \mathbf{v}_{ij}/|\mathbf{v}_{ij}|$. From (22) and (23), the discrete strain energy associated with \mathbf{X}_i is

$$\begin{aligned} E_i &= \frac{k_{ij}}{4} \sum_j \left(\frac{|\mathcal{A}\mathbf{v}_{ij}| - |\mathbf{v}_{ij}|}{d\ell_{ij}} \right)^2 = \frac{k}{4d\ell_{ij}} \sum_{i,j} |\mathbf{v}_{ij}|^2 (|\mathcal{A}\hat{\mathbf{v}}_{ij}| - 1)^2 \\ &= \frac{k_{ij}}{4d\ell_{ij}} \sum_{i,j} |\mathbf{v}_{ij}|^2 (|\mathcal{A}\hat{\mathbf{v}}_{ij}|^2 - 2|\mathcal{A}\hat{\mathbf{v}}_{ij}| + 1) \end{aligned} \quad (\text{A.2})$$

The quadratic term $|\mathcal{A}\hat{\mathbf{v}}_{ij}|^2$ can be expressed as

$$|\mathcal{A}\hat{\mathbf{v}}_{ij}|^2 = \hat{\mathbf{v}}_{ij}^T \mathcal{A}^T \mathcal{A} \hat{\mathbf{v}}_{ij} = 1 + \hat{\mathbf{v}}_{ij}^T \begin{pmatrix} 0 & \gamma \\ \gamma & \gamma^2 \end{pmatrix} \hat{\mathbf{v}}_{ij}. \quad (\text{A.3})$$

The unit vector $\hat{\mathbf{v}}_{ij}$ can be written in polar coordinates as $\hat{\mathbf{v}}_{ij} = (\cos \theta, \sin \theta)^T$. Substituting into Eq. (A.3) yields

$$|\mathcal{A}\hat{\mathbf{v}}_{ij}|^2 = 1 + \gamma (2 \cos \theta \sin \theta + \sin^2 \theta). \quad (\text{A.4})$$

Similarly, the linear term $|\mathcal{A}\hat{\mathbf{v}}_{ij}|$ can be written as

$$|\mathcal{A}\hat{\mathbf{v}}_{ij}| = \sqrt{|\mathcal{A}\hat{\mathbf{v}}_{ij}|^2} = \sqrt{1 + \gamma (2 \cos \theta \sin \theta + \sin^2 \theta)}. \quad (\text{A.5})$$

Expanding this term in the small deformation limit, $\gamma \ll 1$, yields

$$|\mathcal{A}\hat{\mathbf{v}}_{ij}| = 1 + \gamma \cos \theta \sin \theta + \frac{\gamma^2}{2} (\sin^2 \theta - (\cos \theta \sin \theta)^2) + \quad (\text{A.6})$$

$$\frac{\gamma^3}{2} (-\sin^3 \theta \cos \theta + (\cos \theta \sin \theta)^3) + \mathcal{O}(\gamma^4). \quad (\text{A.7})$$

Retaining terms up to $\mathcal{O}(\gamma^2)$, the expression $(|\mathcal{A}\hat{\mathbf{v}}_{ij}| - 1)^2$ simplifies to $(\gamma \cos \theta \sin \theta)^2$. Using the assumption that the network is isotropic, we average over all $\theta \in [0, 2\pi)$,

$$\langle (|\mathcal{A}\hat{\mathbf{v}}_{ij}| - 1)^2 \rangle = \frac{\gamma^2}{2\pi} \int_0^{2\pi} (\cos \theta \sin \theta)^2 d\theta = \frac{\gamma^2}{8}. \quad (\text{A.8})$$

Using this expression and that $|\mathbf{v}_{ij}|^2 \approx \ell_{ij}^2$, the averaged discrete strain energy (A.2) at a point is

$$E_i = \frac{k_{ij}}{4d\ell_{ij}} N_{\text{links}} \left(d\ell_{ij}^2 \frac{\gamma^2}{8} \right) = \frac{3}{16} d\ell_{ij} \gamma^2 k_{ij}, \quad (\text{A.9})$$

where we have assumed that the average number of links to other points is $N_{\text{links}} = 6$.

The strain-energy density function for an isotropic linearly elastic material is

$$W = \frac{\lambda_E}{2} [\text{tr}(\mathcal{E})]^2 + \mu_E \text{tr}(\mathcal{E}^2), \quad (\text{A.10})$$

where the linear strain tensor is

$$\mathcal{E} = \frac{1}{2} (\nabla \mathbf{q} + \nabla \mathbf{q}^T), \quad (\text{A.11})$$

and the displacement vector is

$$\mathbf{q} = \mathbf{X} - \mathbf{x} = \mathcal{A}\mathbf{x} - \mathbf{x}. \quad (\text{A.12})$$

For the shear deformation described above we have

$$\mathbf{q} = \begin{pmatrix} 0 & \gamma \\ 0 & 0 \end{pmatrix} \begin{pmatrix} x \\ y \end{pmatrix} \text{ and } \nabla \mathbf{q} = \begin{pmatrix} 0 & \gamma \\ 0 & 0 \end{pmatrix}. \quad (\text{A.13})$$

The strain tensor is then

$$\mathcal{E} = \frac{1}{2} \begin{pmatrix} 0 & \gamma \\ \gamma & 0 \end{pmatrix}. \quad (\text{A.14})$$

Substituting (A.14) into the strain energy equation (A.10) yields

$$W = \frac{\lambda_E}{2} [\text{tr}(\mathcal{E})]^2 + \mu_E \text{tr}(\mathcal{E}^2) = \frac{\lambda_E}{2} 0^2 + \frac{\mu_E}{4} (2\gamma^2) \quad (\text{A.15})$$

We convert the strain energy density (in 2-D, energy per area) to an energy for comparison to the discrete strain energy. Specifically, we multiply the strain energy density by the area weight of the spring which is given by $(dA_i + dA_j)/2$, where the area weight dA_i at each point \mathbf{X}_i is the sum of one third the area of each triangle with vertex \mathbf{X}_i . Matching the above strain energy to the discrete strain energy for shear deformations, we obtain

$$(\mu_E \gamma^2 / 2) (dA_i + dA_j) / 2 = 3k_{ij} \gamma^2 d\ell_{ij} / 16, \quad (\text{A.16})$$

and

$$k_{ij} = \frac{8\mu_E}{3d\ell_{ij}} \left(\frac{dA_i + dA_j}{2} \right). \quad (\text{A.17})$$

Bulk Modulus

The bulk modulus in three dimensions is related to the Lamé constants by $K_v = \lambda_E + 2\mu_E/3$ and by $K_v = \lambda_E + \mu_E$ in two dimensions. To determine λ_E (and the bulk modulus), we consider a pure compression deformation so that the deformation gradient is

$$\mathcal{A} = \begin{pmatrix} 1 + \gamma & 0 \\ 0 & 1 + \gamma \end{pmatrix}. \quad (\text{A.18})$$

We compute the terms $|\mathcal{A}\hat{\mathbf{v}}_{ij}|$ and $|\mathcal{A}\hat{\mathbf{v}}_{ij}|^2$ that appear in (A.2) for the compressive deformation (A.18). The quadratic term is

$$|\mathcal{A}\hat{\mathbf{v}}_{ij}|^2 = \hat{\mathbf{v}}_{ij}^T \mathcal{A}^T \mathcal{A} \hat{\mathbf{v}}_{ij} = \hat{\mathbf{v}}_{ij}^T \begin{pmatrix} (1 + \gamma)^2 & 0 \\ 0 & (1 + \gamma)^2 \end{pmatrix} \hat{\mathbf{v}}_{ij} = (1 + \gamma)^2, \quad (\text{A.19})$$

and the linear term is

$$|\mathcal{A}\hat{\mathbf{v}}_{ij}| = (1 + \gamma). \quad (\text{A.20})$$

The averaged discrete strain energy at the point \mathbf{X}_i is

$$E_i = \frac{k_{ij}}{4d\ell_{ij}} \sum_{i,j} |\mathbf{v}_{ij}|^2 \gamma^2 = \frac{k_{ij}}{4} d\ell_{ij} \gamma^2 \times N_{\text{links}} = \frac{3}{2} k_{ij} d\ell_{ij} \gamma^2, \quad (\text{A.21})$$

where again we take the average number of links at a point to be 6.

The strain tensor is simply $\mathcal{E} = \gamma \mathcal{I}$, and so from Eq. (A.10) the strain energy density is

$$W = \left(\frac{\lambda_E}{2} (4\gamma^2) + 2\mu_E \gamma^2 \right) = 2\gamma^2 (\lambda_E + \mu_E). \quad (\text{A.22})$$

Multiplying by the area weight, the elastic deformation energy at a point is

$$E = 2\gamma^2 (\lambda_E + \mu_E) \left(\frac{dA_i + dA_j}{2} \right) = \frac{3}{2} k_{ij} d\ell_{ij} \gamma^2. \quad (\text{A.23})$$

Taking the shear modulus from above, $\mu_E = 3k_{ij}d\ell_{ij}/(4(dA_i + dA_j))$, and solving for λ_E gives

$$\lambda_E = \frac{3}{2} \frac{k_{ij}d\ell_{ij}}{(dA_i + dA_j)} - \frac{3}{4} \frac{k_{ij}d\ell_{ij}}{(dA_i + dA_j)} = \frac{3}{4} \frac{k_{ij}d\ell_{ij}}{(dA_i + dA_j)}. \quad (\text{A.24})$$

Note that $\lambda_E = \mu_E$, and thus a single elastic modulus characterizes the elastic material. The bulk modulus necessarily equals $2\mu_E$ in two dimensions. We conclude that

$$k_{ij} = \frac{8\lambda_E}{3d\ell_{ij}} \left(\frac{dA_i + dA_j}{2} \right). \quad (\text{A.25})$$

Appendix B. Linear vs. Nonlinear Elasticity

In this appendix, we compare simulation results for linear and nonlinear elastic models using the energy-based framework described in Section 2.3. It is important to note that linear elasticity is not frame invariant, meaning that the stresses are not independent of the coordinate system. Said another way, a rigid rotation potentially generates elastic stress in a linearly elastic model. In biological applications, large deformations are not uncommon, particularly for soft materials such as cytoskeleton. Here we demonstrate that a linearly elastic model can produce spurious torque and artificial rotation when the material experiences large deformations.

We use the same test problem from Section 3: a circular elastic structure is initially expanded uniformly in the radial direction and allowed to relax back to rest. Parameters in the following simulations are identical those in Section 3, except that here the initial structure is expanded by 25%, in comparison to the expansion of 0.01% presented in Section 3. We use a compressible neo-Hookean model for nonlinear elasticity with strain energy given by (20), and the strain energy function for linear elasticity is given by (21).

In this test, we expect motion of the elastic structure only in the radial direction and the fluid velocity to be zero. The torque density should be zero at every point throughout the simulation because the deformation and motion is only in the radial direction. We compute the net torque on the structure by

$$\tau = \int_{\Gamma} \mathbf{X} \times \mathbf{F}_{\text{elastic}}^{\text{net}} ds. \quad (\text{B.1})$$

The maximum net torque over the simulation for different grids is shown in Fig.12(a). These data show that the net torque is not zero in the computations involving linear elasticity, and the size of the net torque increases as the grid is refined, while the torques produced by the neo-Hookean model are zero to

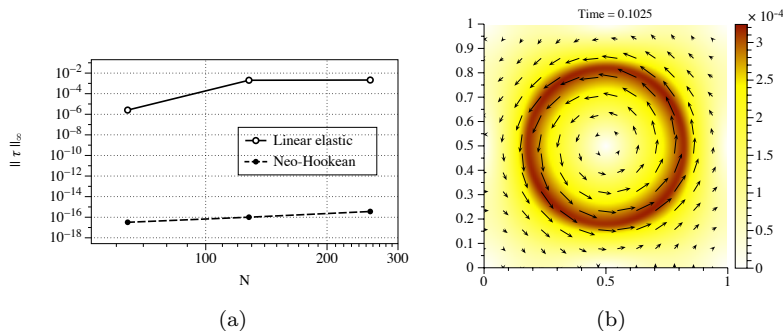


Figure B.12: (a) Maximum of the net torque for linear and neo-Hookean elastic models for simulations from $t = 0$ to $t = 0.5$. (b) Example of a velocity field (arrows) and its magnitude (color field) during the simulation using the linearly elastic model on a 128×128 grid.

machine accuracy. The spurious torques generated with the linearly elastic model produce an unphysical rotational flow, as demonstrated by the example flow field in Fig. 12(b).

Next, we assess the affect of the rotational flow on the motion of the structure. The displacement vector field was converted into polar coordinates with components (q_r, q_θ) . The size of the angular displacement, q_θ , quantifies the rotation of the material, and its maximum value over time is plotted in Fig. B.13 for the two different elasticity models. For this simulation, we expect the displacement in the θ -direction to be zero. The angular displacement is very small and well below discretization errors for the neo-Hookean model for nonlinear elasticity, but it is several orders of magnitude larger for linear elasticity. The angular displacement for the nonlinear material arises simply from discretization errors; the mesh is not radially symmetric, and so the discrete solution is not perfectly symmetric. For the linearly elastic material, the angular displacement grows in time and reaches a value which is about 10% of the original radial displacement. This large error is the product of the spurious torque and resulting rotational flow.

The data presented in this appendix indicates that linear elasticity should only be used for small deformations when using the energy-based method. However, there is no reason to use linear elasticity even for small deformations because nonlinear constitutive laws do not introduce any additional complexity to the method.

References

- [1] C. S. Peskin, Numerical analysis of blood flow in the heart, *J. Comput. Phys.* 25 (3) (1977) 220–252.
- [2] L. A. Miller, C. S. Peskin, When vortices stick: an aerodynamic transition in tiny insect flight, *J. Exp. Biol.* 207 (2004) 3073–3088.

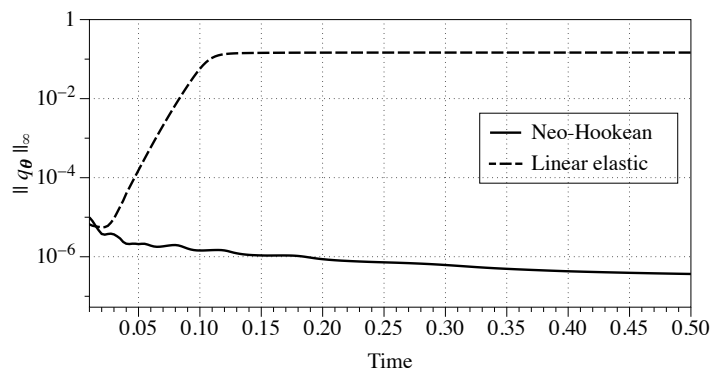


Figure B.13: Maximum displacement in the θ -direction over time for the linear and nonlinear models. Displacement is expected to be nonzero only in the radial component.

- [3] L. J. Fauci, C. S. Peskin, A computational model of aquatic animal locomotion, *J. Comput. Phys.* 77 (1) (1988) 85–108.
- [4] Y. Kim, C. S. Peskin, 2-D parachute simulation by the immersed boundary method, *SIAM J. Sci. Comput.* 28 (6) (2006) 2294–2312.
- [5] J. M. Stockie, Modelling and simulation of porous immersed boundaries, *Comput. Struct.* 87 (2009) 701–709.
- [6] C. Hamlet, A. Santhanakrishnan, L. A. Miller, A numerical study of the effects of bell pulsation dynamics and oral arms on the exchange currents generated by the upside-down jellyfish *cassiopea xamachana*, *J. Exp. Biol.* 214 (2011) 1911–1921.
- [7] D. Boffi, L. Gastaldi, L. Heltai, C. S. Peskin, On the hyper-elastic formulation of the immersed boundary method, *Comput. Method. Appl. M.* 197 (25-28) (2008) 2210–2231.
- [8] B. E. Griffith, X. Luo, Immersed boundary method with finite element elasticity, available from http://www.cims.nyu/~docs/griffith_ibfem_sub.pdf.
- [9] D. Devendran, C. S. Peskin, An immersed boundary energy-based method for incompressible viscoelasticity, *J. Comput. Phys.* 231 (14) (2012) 4613 – 4642.
- [10] G. T. Charras, J. C. Yarrow, M. A. Horton, L. Mahadevan, T. J. Mitchison, Non-equilibration of hydrostatic pressure in blebbing cells, *Nature* 435 (7040) (2005) 365–369.

- [11] S. Sivaloganathan, M. Stastna, G. Tenti, J. Drake, Biomechanics of the brain: A theoretical and numerical study of biot’s equations of consolidation theory with deformation-dependent permeability, *Int. J. Nonlin. Mech.* 40 (9) (2005) 1149–1159.
- [12] K. Leiderman, A. L. Fogelson, The influence of hindered transport on the development of platelet thrombi under flow, *Bull. Math. Biol.* 75 (8) (2012) 1255–1283.
- [13] B. Alberts, A. Johnson, J. Lewis, M. Raff, K. Roberts, P. Walter, *Molecular biology of the cell*, 4th Edition, Garland Science, New York, 2002.
- [14] W. Alt, M. Dembo, Cytoplasm dynamics and cell motion: two-phase flow models, *Math. Biosci.* 156 (1-2) (1999) 207–228.
- [15] M. Gracheva, H. Othmer, A continuum model of motility in ameboid cells, *B. Math. Biol.* 66 (2004) 167–193.
- [16] M. R. K. Mofrad, Rheology of the cytoskeleton, *Annu. Rev. Fluid Mech.* 41 (2009) 433–453.
- [17] O. T. Fackler, R. Grosse, Cell motility through plasma membrane blebbing, *J. Cell Biol.* 181 (6) (2008) 879–884.
- [18] G. Charras, E. Paluch, Blebs lead the way: how to migrate without lamellipodia, *Nat. Rev. Mol. Cell Biol.* 9 (9) (2008) 730–736.
- [19] J. Y. Tinevez, U. Schulze, G. Salbreux, J. Roensch, J. F. Joanny, E. Paluch, Role of cortical tension in bleb growth, *Proc. Natl. Acad. Sci. USA* 106 (44) (2009) 18581–18586.
- [20] A. Grebecki, Membrane and cytoskeleton flow in motile cells with emphasis on the contribution of free-living amoebae, *Int. Rev. Cytol.* 148 (37-80).
- [21] K. Matsumoto, S. Takagi, T. Nakagaki, Locomotive Mechanism of Physarum Plasmodia Based on Spatiotemporal Analysis of Protoplasmic Streaming, *Biophys. J.* 94 (7) (2008) 2492–2504.
- [22] N. G. Cogan, R. D. Guy, Multiphase flow models of biogels from crawling cells to bacterial biofilms, *HFSP Journal* 4 (1) (2010) 11–25.
- [23] M. A. Biot, General theory of three-dimensional consolidation, *Journal of Applied Physics* 12 (2) (1941) 155–164.
- [24] A. J. Levine, F. C. MacKintosh, The mechanics and fluctuation spectrum of active gels, *J. Phys. Chem. B* 113 (12) (2009) 3820–3830.
- [25] R. Ogden, *Nonlinear Elastic Deformations*, Courier Dover Publications, 1997.

- [26] L. E. Malvern, *Introduction to the Mechanics of a Continuous Medium*, 1st Edition, Prentice Hall, 1977.
- [27] C. S. Peskin, The immersed boundary method, *Acta Numer.* 11 (2002) 479–517.
- [28] M. Ostoja-Starzewski, Lattice models in micromechanics, *Appl. Mech. Rev.* 55 (1) (2002) 35–60.
- [29] A. Hrennikoff, Solution of problems of elasticity by the framework method, *J. App. Mech.* 8 (4) (1941) 169–175.
- [30] P. Meakin, A simple model for elastic fracture in thin films, *Thin Solid Films* 151 (2) (1987) 165–190.
- [31] W. Curtin, H. Scher, Mechanics modelling using a spring network, *J. Mater. Res.* 5 (3) (1990) 554–562.
- [32] Y. Termonia, P. Meakin, Formation of fractal cracks in a kinetic fracture model, *Nature* 320 (6061) (1986) 429–431.
- [33] H. Herrmann, J. Kertész, L. De Arcangelis, Fractal shapes of deterministic cracks, *Europhys. Lett.* 10 (2) (1989) 147.
- [34] G. N. Hassold, D. J. Srolovitz, Brittle fracture in materials with random defects, *Phys. Rev. B* 39 (1989) 9273–9281.
- [35] G.-F. Zhao, J. Fang, J. Zhao, A mls-based lattice spring model for simulating elasticity of materials, *Int. J. of Comput. Methods* 9 (3).
- [36] P. Persson, G. Strang, A simple mesh generator in matlab, *SIAM Rev.* 46 (2) (2004) 329–345.
- [37] W. Liu, Y. Liu, D. Farrell, L. Zhang, X. Wang, Y. Fukui, N. Patankar, Y. Zhang, C. Bajaj, J. Lee, J. Hong, X. Chen, H. Hsu, Immersed finite element method for fluid-structure interactions, *Comput. Meth. Appl. Mech. Eng.* 195 (13-16) (2006) 1722–1749.
- [38] L. Zhang, M. Gay, Immersed finite element method for fluid-structure interactions, *J. Fluid Struct* 23 (6) (2007) 839–857.
- [39] B. Maugis, J. Brugués, P. Nassoy, N. Guillen, P. Sens, F. Amblard, Dynamic instability of the intracellular pressure drives bleb-based motility, *J. Cell Sci.* 123 (Pt 22) (2010) 3884–92.
- [40] A. Diz-Muñoz, M. Krieg, M. Bergert, I. Ibarlucea-Benitez, D. J. Muller, E. Paluch, C. P. Heisenberg, Control of directed cell migration in vivo by membrane-to-cortex attachment, *PLOS Biol.* 8 (11) (2010) e1000544.

- [41] K. Wolf, I. Mazo, H. Leung, K. Engelke, U. H. von Andrian, E. I. Deryugina, A. Y. Strongin, E. B. Bröcker, P. Friedl, Compensation mechanism in tumor cell migration: mesenchymal-amoeboid transition after blocking of pericellular proteolysis, *J. Cell Biol.* 160 (2) (2003) 267–277.
- [42] W. Strychalski, R. D. Guy, A computational model of bleb formation, *Math. Med. Biol.* 30 (2) (2013) 115–130.
- [43] J. Stricker, T. Falzone, M. L. Gardel, Mechanics of the F-actin cytoskeleton, *J. Biomech.* 43 (1) (2010) 9–14.
- [44] T. D. Pollard, G. C. Borisy, Cellular motility driven by assembly and disassembly of actin filaments, *Cell* 112 (4) (2003) 453–465.
- [45] H. Aldrich, *Cell Biology of Physarum and Didymium V1: Organisms, Nucleus, and Cell Cycle*, Access Online via Elsevier, 1982.
- [46] R. D. Guy, B. Philip, A multigrid method for a model of the implicit immersed boundary equations, *Commun. Comput. Phys.* 12 (2012) 378–400.
- [47] H. D. Ceniceros, J. E. Fisher, A fast, robust, and non-stiff immersed boundary method, *J. Comput. Phys.* 230 (12) (2011) 5133–5153.
- [48] E. P. Newren, A. L. Fogelson, R. D. Guy, R. M. Kirby, A comparison of implicit solvers for the immersed boundary equations, *Comput. Methods Appl. Mech. Engrg.* 197 (25-28) (2008) 2290–2304.
- [49] E. P. Newren, A. L. Fogelson, R. D. Guy, R. M. Kirby, Unconditionally stable discretizations of the immersed boundary equations, *J. Comput. Phys.* 222 (2) (2007) 702–719.
- [50] Y. Mori, C. S. Peskin, Implicit second-order immersed boundary methods with boundary mass, *Comput. Methods Appl. Mech. Engrg.* 197 (25-28) (2008) 2049 – 2067.
- [51] T. Y. Hou, Z. Shi, An efficient semi-implicit immersed boundary method for the navier-stokes equations, *J. Comput. Phys.* 227 (20) (2008) 8968–8991.
- [52] H. D. Ceniceros, J. E. Fisher, A. M. Roma, Efficient solutions to robust, semi-implicit discretizations of the immersed boundary method, *J. Comput. Phys.* 228 (19) (2009) 7137–7158.